

Controlling vanadium phosphate catalyst precursor morphology by adding alkane solvents in the reduction step of $\text{VOPO}_4 \cdot 2\text{H}_2\text{O}$ to $\text{VOHPO}_4 \cdot 0.5\text{H}_2\text{O}$ †

Weihao Weng,^a Raja Al Otaibi,^b Mosaed Alhumaimess,^b Marco Conte,^b Jonathan K. Bartley,^b Nicholas F. Dummer,^b Graham J. Hutchings^b and Christopher J. Kiely^{*a}

Received 31st May 2011, Accepted 17th August 2011

DOI: 10.1039/c1jm12456k

Vanadium phosphate catalysts were prepared by reducing square $\text{VOPO}_4 \cdot 2\text{H}_2\text{O}$ platelets with n-octane and 1-butanol and the resultant materials were characterized using a combination of techniques including powder X-ray diffraction and electron microscopy. The specific order in which the alkane and alcohol are added during the reduction step was found to have a remarkable influence on the precursor morphology and eventual catalytic activity of the final $(\text{VO})_2\text{P}_2\text{O}_7$ catalyst. Without the addition of n-octane the product consists of typical rosette-type $\text{VOHPO}_4 \cdot 0.5\text{H}_2\text{O}$ and n-octane addition after the reduction step does not significantly change the precursor morphology. By way of contrast, the addition of the n-octane before the reduction step leads to the formation of octagonal $\text{VOPO}_4 \cdot 2\text{H}_2\text{O}$ platelets which are then subsequently reduced by 1-butanol to form nanoscale rhomboidal $\text{VOHPO}_4 \cdot 0.5\text{H}_2\text{O}$ platelets. The co-addition of n-octane and 1-butanol, on the other hand, can reduce and reform the square $\text{VOPO}_4 \cdot 2\text{H}_2\text{O}$ crystals into rosette-type aggregates of angular $\text{VOHPO}_4 \cdot 0.5\text{H}_2\text{O}$ platelets. Nearly all of the catalysts generated exhibit a high activity and selectivity to maleic anhydride. The only exception is the catalyst produced by activating the nanoscale rhomboidal morphology precursor, which is attributed to its poorer crystallinity and more limited exposure of the active (100) $(\text{VO})_2\text{P}_2\text{O}_7$ plane. Furthermore, the spatial orientation relationship between the starting $\text{VOPO}_4 \cdot 2\text{H}_2\text{O}$ crystal and the $\text{VOHPO}_4 \cdot 0.5\text{H}_2\text{O}$ precursor phase has been identified in this study as $[001]^{\text{VOPO}_4 \cdot 2\text{H}_2\text{O}} // [001]^{\text{VOHPO}_4 \cdot 0.5\text{H}_2\text{O}}$ and $[100]^{\text{VOPO}_4 \cdot 2\text{H}_2\text{O}} // [110]^{\text{VOHPO}_4 \cdot 0.5\text{H}_2\text{O}}$. This information leads us to propose a two-step mechanism by which the topotactic transformation of $\text{VOPO}_4 \cdot 2\text{H}_2\text{O}$ to $\text{VOHPO}_4 \cdot 0.5\text{H}_2\text{O}$ occurs.

1. Introduction

Vanadium phosphate (V-P-O) catalysts are used commercially for the selective oxidation of n-butane to maleic anhydride (MA), and represent one of the most well studied heterogeneous mixed oxide catalyst systems.^{1–18} It is generally accepted that vanadyl pyrophosphate ($(\text{VO})_2\text{P}_2\text{O}_7$) is the active phase, which is obtained by activating the catalyst precursor, vanadyl hydrogen phosphate hemihydrate ($\text{VOHPO}_4 \cdot 0.5\text{H}_2\text{O}$) under the reaction conditions.^{1–3} Since the activated catalyst is formed topotactically from the precursor,^{3–5} controlling the morphology of the precursor through the preparation route is an important parameter in generating a material which has a high catalytic performance.

In view of the importance of controlling the morphology of the catalyst precursor, numerous studies have been reported.^{6–11} Commonly, V_2O_5 is used as the vanadium source and H_3PO_4 is used as the phosphorus source; a suitable reducing agent is then required to synthesize the $\text{VOHPO}_4 \cdot 0.5\text{H}_2\text{O}$ (V^{4+}) precursor phase. A number of different reducing agents and solvents have been tried in this respect.^{12,13} In the earliest reported V-P-O catalyst preparation method (denoted as the VPA route) water was used as the solvent and hydrochloric acid was used as the reducing agent.^{14,15} More recently, studies have concentrated on the use of alcohols as solvents and reducing agents, (*i.e.*, the VPO and VPD routes) as they tend to result in higher surface area catalysts.^{14,16} The VPD method was first described by Johnson *et al.*⁵ and later refined by Horowitz *et al.*¹⁷ and Ellison *et al.*¹⁸ This method involves the reaction of V_2O_5 with H_3PO_4 using water as the solvent, which leads to the formation of the V^{5+} vanadium phosphate dihydrate $\text{VOPO}_4 \cdot 2\text{H}_2\text{O}$ phase, that is subsequently reduced in a second stage using an alcohol as the reducing agent to form the $\text{VOHPO}_4 \cdot 0.5\text{H}_2\text{O}$ precursor. The $\text{VOPO}_4 \cdot 2\text{H}_2\text{O}$ phase has a layer-type structure in which the VO_6 octahedra share their equatorial oxygen atoms with the PO_4 tetrahedra and each of the

^aDepartment of Materials Science and Engineering, Lehigh University, Bethlehem, PA, 18015-3195, USA. E-mail: chk5@lehigh.edu

^bCardiff Catalysis Institute, School of Chemistry, Cardiff University, Cardiff, CF10 3AT, UK

† Electronic supplementary information (ESI) available. See DOI: 10.1039/c1jm12456k

VOPO₄ sheets are connected by interlayer water molecules.¹⁹ Hence the VOPO₄·2H₂O crystal is able, *via* water displacement, to accommodate organic molecules of various types between the layers, yielding a number of intercalation type compounds incorporating amine,²⁰ amide²¹ and alcohol molecules.²²

More recently, Okuhara *et al.*¹² have reported the intercalation and subsequent exfoliation and fracture of VOPO₄·2H₂O crystals using primary and secondary alcohols. This was achieved *via* low temperature heating in the alcohol followed by a subsequent reduction step in which the exfoliated VOPO₄·2H₂O sheets fracture to yield a VOHPO₄·0.5H₂O precursor which had a distinctive nano-sized (~ 340 × 35 nm) blocky morphology. In addition, the nanocrystalline (VO)₂P₂O₇ catalyst subsequently derived from this precursor was found to be highly active and selective for the oxidation n-butane to MA.²³

Recently we have shown that the addition of an alkane co-solvent to the alcohol at the reduction stage in the VPD route can significantly influence the crystallinity and morphology of the resulting catalyst precursor.⁹ The amount of alkane added to the primary alcohol (*i.e.*, 1-octanol), determined whether the VOPO₄·2H₂O materials were transformed into VO(H₂PO₄)₂ with a blocky morphology, VOHPO₄·0.5H₂O with a platelet morphology, or VOHPO₄·0.5H₂O with a rosette-type morphology. These crystal structure and morphological changes were shown to depend on the precise alcohol:alkane volume ratio in the reduction step. In this study, vanadium phosphate catalysts have been prepared by reducing VOPO₄·2H₂O with n-octane and 1-butanol in an autoclave reactor. The specific *order* in which the alkane and alcohol are added during the reaction is shown to have a profound effect on the precursor morphology and eventual catalytic activity of the final (VO)₂P₂O₇ phase. Furthermore, through this study we have been able to elucidate the spatial orientation relationship between the VOPO₄·2H₂O and VOHPO₄·0.5H₂O crystalline phases. This information has enabled us to propose a mechanism by which the important VOPO₄·2H₂O to VOHPO₄·0.5H₂O topotactic transformation occurs.

2. Experimental

2.1 Catalyst preparation

Preparation of VOPO₄·2H₂O. V₂O₅ (10 g, Aldrich) and H₃PO₄ (60 ml, 85%, Aldrich) were heated in distilled water (120 ml) under reflux conditions for 24 h. The yellow solid was recovered immediately by vacuum filtration, washed with cold distilled water (100 ml) and acetone (100 ml) and dried in air at 110 °C for 24 h.

Reaction of VOPO₄·2H₂O with 1-butanol followed by n-octane (Route A). The VOPO₄·2H₂O (2 g) was reacted with 1-butanol (46 ml) in an autoclave at 150 °C (autogeneous pressure) for 24 h. The resultant solid was recovered by vacuum filtration, and then washed with acetone (100 ml) and dried in air at 110 °C. Some of this recovered solid was returned to the autoclave with n-octane (46 ml) and heated at 150 °C (autogeneous pressure) for a further 24 h. The final solid generated was again recovered by vacuum filtration, and then washed with acetone (100 ml) and dried in air at 110 °C.

Reaction of VOPO₄·2H₂O with n-octane followed by 1-butanol (Route B). The VOPO₄·2H₂O (2 g) was reacted with n-octane (46 ml) in an autoclave at 150 °C (autogeneous pressure) for 24 h. The resultant solid was recovered by vacuum filtration, and then washed with acetone (100 ml) and dried in air at 110 °C. Some of the recovered solid was then returned to the autoclave with 1-butanol (46 ml) and heated at 150 °C (autogeneous pressure) for a further 24 h. The final solid generated was again recovered by vacuum filtration, and then washed with acetone (100 ml) and dried in air at 110 °C.

Reaction of VOPO₄·2H₂O with (1 : 1 n-octane:1-butanol mixture) (Route C). The VOPO₄·2H₂O (2 g) was reacted with 1-butanol (23 ml) and n-octane (23 ml) in an autoclave at 150 °C (autogeneous pressure) for 24 h. The resultant solid was recovered by vacuum filtration, and then washed with acetone (100 ml) and dried in air at 110 °C.

2.2 Catalyst characterization

A number of complementary techniques were used to structurally characterize the materials produced. Powder X-ray diffraction (XRD) was performed using a Panatytical X'pert Pro X-ray diffractometer using Cu K_α radiation operating at 40 mA and 40 kV. BET surface area measurements by nitrogen adsorption at -196 °C were conducted with a Micromeritics ASAP 2010 instrument. Samples were degassed for 1 h at 120 °C prior to analysis. Laser Raman spectra were obtained on a Renishaw System 1000 Raman-scoped spectrograph fitted with a green Argon ion (Ar⁺) laser (λ = 514.532 nm).

Samples for scanning electron microscopy (SEM) analyses were mounted onto an aluminium stub using carbon tape and sputtered with iridium to mitigate the effects of sample charging. SEM analyses were performed on a Hitachi S-4300LV microscope equipped with a Schottky field emission gun. Samples were prepared for transmission electron microscopy (TEM) examination by grinding the powders between clean glass slides and then dispersing them onto a lacey carbon film supported on a Cu mesh grid. Bright field transmission electron microscopy (BF-TEM) and selected area electron diffraction (SAED) experiments were carried out using a JEOL 2000FX microscope equipped with a thermionic LaB₆ source operating at 200 kV.

2.3 Catalyst testing

The oxidation of n-butane was carried out in a fixed bed micro-reactor with a standard mass of catalyst (0.2 g). n-Butane and air were introduced into the reactor *via* calibrated mass flow controllers to give a feedstock composition of 1.7% n-butane in air. Catalyst precursor samples were activated *in-situ* by heating the sample from room temperature to 400 °C at a rate of 3 °C/min. The reaction products were fed *via* heated lines to an on-line gas chromatograph for analysis. The reactor comprised a stainless steel tube with the catalyst held in place by plugs of quartz wool. A thermocouple was located in the centre of the catalyst bed and temperature control was typically better than

± 1 °C. Carbon mass balances of 97–103% were typically observed.

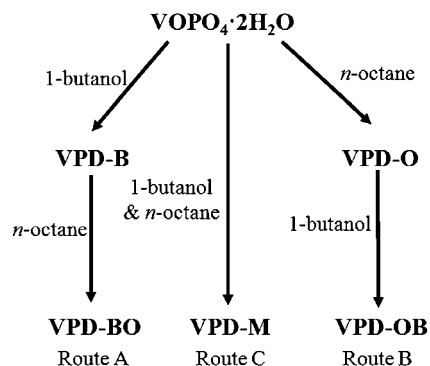
3. Results

Characterization of the starting $\text{VOPO}_4 \cdot 2\text{H}_2\text{O}$ material

The standard $\text{VOPO}_4 \cdot 2\text{H}_2\text{O}$ (V^{5+}) material prepared using the VPD route typically consists of square platelets (Fig. 1(a)) that range from 4–60 μm in size and 0.2–1.0 μm in thickness and exhibit a layer-type structure (Fig. 1(b)). The surface area of such materials is typically about $1 \text{ m}^2\text{g}^{-1}$. Selected area electron diffraction (SAED) patterns obtained from the platelet normal direction (Fig. 1(d)) can be indexed to the [001] projection of the tetragonal $\text{VOPO}_4 \cdot 2\text{H}_2\text{O}$ phase (Fig. 1(e)).¹⁹ The termination facets of the square platelets, each with a 90° intersection angle, correspond to alternating $\{110\}$ -type planes around the [001] axis of $\text{VOPO}_4 \cdot 2\text{H}_2\text{O}$ (Fig. 1(c)). The XRD patterns (Fig. 1(f)) of this material show that all the peaks can be assigned to $\text{VOPO}_4 \cdot 2\text{H}_2\text{O}$ with the dominant reflection at 12.1° (d -spacing = 7.27 Å) corresponding to the (001) plane.

Starting from the standard square $\text{VOPO}_4 \cdot 2\text{H}_2\text{O}$ material, three different reaction protocols, denoted as routes A, B and C,

were used to generate catalyst precursors $\text{VOHPO}_4 \cdot 0.5\text{H}_2\text{O}$ (V^{4+}) as shown in Scheme 1. The primary difference between these routes is the order in which the 1-butanol and *n*-octane has been added to the $\text{VOPO}_4 \cdot 2\text{H}_2\text{O}$ slurry. In route A, 1-butanol was added first, followed by *n*-octane. In route B, the sequence is reversed *i.e.* *n*-octane was added first followed by 1-butanol. In



Scheme 1 Schematic diagram summarizing the various combinations of alcohol and alkane addition during the dehydration of $\text{VOPO}_4 \cdot 2\text{H}_2\text{O}$ explored in this work.

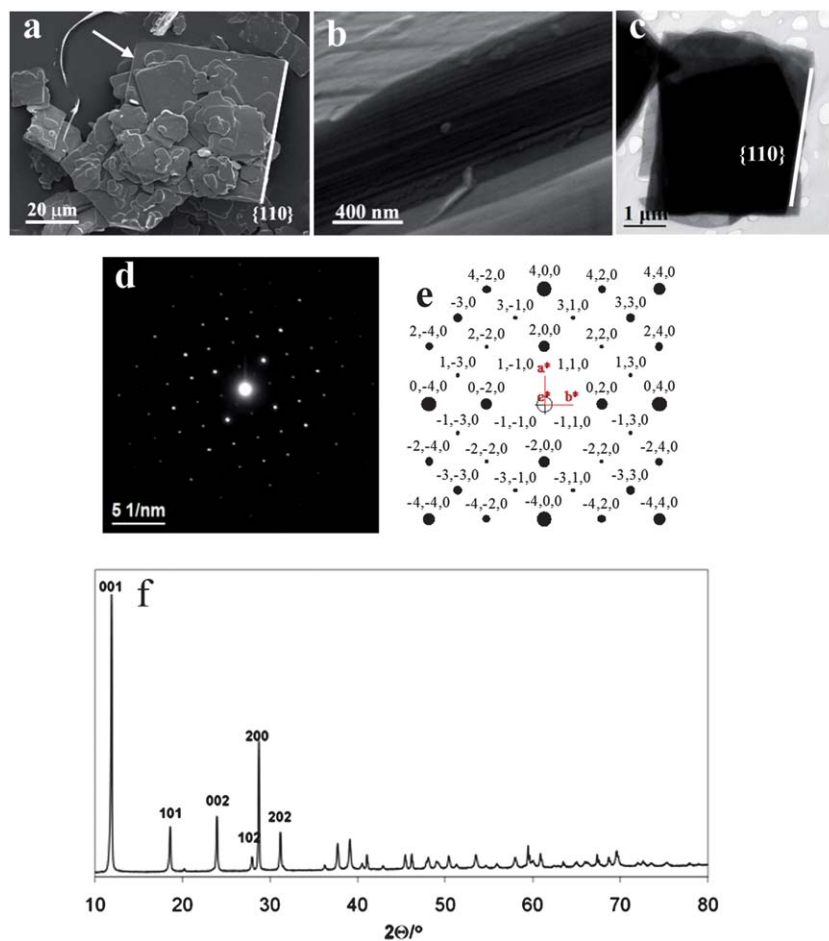


Fig. 1 SEM micrographs of standard $\text{VOPO}_4 \cdot 2\text{H}_2\text{O}$ crystals showing (a) their square platelet morphology and (b) an edge-on view of their layer-type structure; (c) BF-TEM micrograph of a $\text{VOPO}_4 \cdot 2\text{H}_2\text{O}$ platelet showing $\{110\}$ -type termination facets, (d) its corresponding SAED pattern which matches to the [001] projection of $\text{VOPO}_4 \cdot 2\text{H}_2\text{O}$ and (e) simulated and indexed SAED pattern in the [001] projection of $\text{VOPO}_4 \cdot 2\text{H}_2\text{O}$; (f) typical XRD pattern obtained from the $\text{VOPO}_4 \cdot 2\text{H}_2\text{O}$ material.

the route C preparation, both n-octane and 1-butanol were added simultaneously to the $\text{VOPO}_4 \cdot 2\text{H}_2\text{O}$ slurry.

XRD characterization of the $\text{VOHPO}_4 \cdot 0.5\text{H}_2\text{O}$ materials derived through routes A, B and C

Fig. 2 shows the XRD patterns of the final precursor materials (VPD-B, VPD-BO, VPD-OB and VPD-M) generated *via* routes A, B and C respectively. In each case, all the reflections can be indexed to $\text{VOHPO}_4 \cdot 0.5\text{H}_2\text{O}$. This phase identification was confirmed by Raman spectroscopy (Fig. S1, ESI†). The predominant (220) reflection in the XRD spectrum from sample VPD-B is characteristic of the rosette-type precursor morphology usually prepared by the standard VPD route using 1-butanol as the reducing agent. After refluxing with n-octane, precursor VPD-BO remained crystalline $\text{VOHPO}_4 \cdot 0.5\text{H}_2\text{O}$, as determined by XRD, showing a similar XRD pattern to that of material VPD-B, indicating that n-octane does not further alter the crystalline structure of $\text{VOHPO}_4 \cdot 0.5\text{H}_2\text{O}$. In route B when the starting $\text{VOPO}_4 \cdot 2\text{H}_2\text{O}$ material was mixed with n-octane to form VPD-O, it retained its $\text{VOPO}_4 \cdot 2\text{H}_2\text{O}$ crystalline structure (XRD not shown; additional Raman Spectroscopic evidence is included in Fig. S2†). The subsequent reduction of sample VPD-O in 1-butanol generates a material whose dominant reflection in the $\text{VOHPO}_4 \cdot 0.5\text{H}_2\text{O}$ XRD pattern is no longer (220) but instead is (001). The high (001)/(220) peak ratio in the XRD spectrum of VPD-OB is typical of a platelet (as opposed to rosette) type morphology $\text{VOHPO}_4 \cdot 0.5\text{H}_2\text{O}$ material. This indicates that the $\text{VOPO}_4 \cdot 2\text{H}_2\text{O}$ material treated with n-octane (VPD-O) undergoes a different reduction process in route B compared to route A, where the $\text{VOPO}_4 \cdot 2\text{H}_2\text{O}$ material has already converted to $\text{VOHPO}_4 \cdot 0.5\text{H}_2\text{O}$ before it is refluxed with n-octane. For route C, the precursor material VPD-M, which was prepared by *co-addition* of n-octane and 1-butanol, exhibits an XRD pattern that bears some similarities to that of precursor VPD-OB but with a lower (001)/(220) peak ratio. This suggests that it adopts a structure which is intermediate between that of the classic rosette and platelet $\text{VOHPO}_4 \cdot 0.5\text{H}_2\text{O}$ morphologies.

Electron microscopy characterization of route A materials

In the first step, the reaction of $\text{VOPO}_4 \cdot 2\text{H}_2\text{O}$ with 1-butanol in route A gave rise to a typical rosette-type agglomerate (VPD-B,

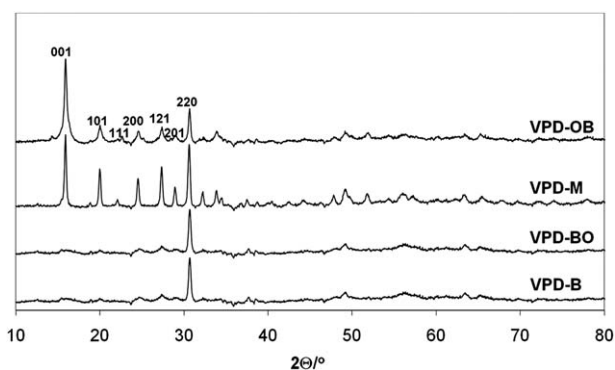


Fig. 2 Powder XRD patterns of catalyst precursors VPD-B, VPD-BO, VPD-OB and VPD-M prepared by routes A, B and C, respectively (All the reflections can be indexed to $\text{VOHPO}_4 \cdot 0.5\text{H}_2\text{O}$).

Fig. 3(a)) in good agreement with the corresponding XRD pattern (Fig. 2, VPD-B). TEM and SAED analysis of a single ‘petal’ crystallite from one of the rosettes is shown in Fig. 3(b), (c). The ‘petal’ had (220)-type termination facets and a normal direction which corresponded to the [001] projection of $\text{VOHPO}_4 \cdot 0.5\text{H}_2\text{O}$.^{16,24} The second step in the preparation procedure (*i.e.* the addition of n-octane) does not further change the crystal structure of the material. The VPD-BO sample is also the $\text{VOHPO}_4 \cdot 0.5\text{H}_2\text{O}$ phase (Fig. 3(f)) showing a similar rosette-type morphology (Fig. 3(d)) to that of VPD-B. Meanwhile the surface area (Table 1) decreases from $27 \text{ m}^2 \text{ g}^{-1}$ for VPD-B to $18 \text{ m}^2 \text{ g}^{-1}$ for VPD-BO after refluxing with n-octane, which could be correlated with the formation of a coarser rosette-type structure.

Electron microscopy characterization of route B materials

Refluxing $\text{VOPO}_4 \cdot 2\text{H}_2\text{O}$ with n-octane as the first step was found to change the morphology of the $\text{VOPO}_4 \cdot 2\text{H}_2\text{O}$ from square platelets (Fig. 1(a)) to octagonal platelets (Fig. 4(a)).

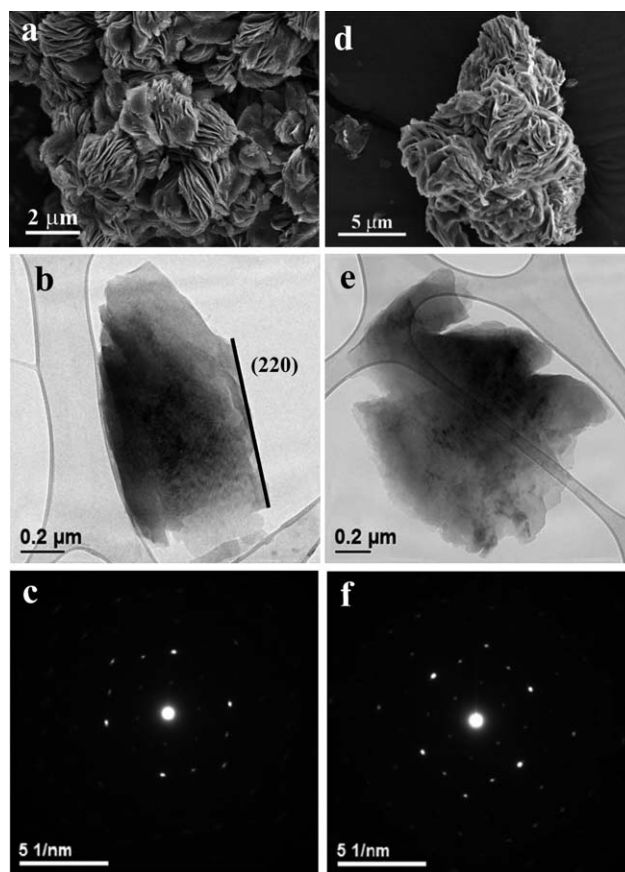


Fig. 3 (a, b, c) VPD-B intermediate material: (a) SEM micrograph showing a characteristic rosette-type morphology; (b) BF-TEM micrograph showing a single ‘petal’ from the rosette agglomerate having (220)-type termination facets; and (c) SAED pattern from the ‘petal’ in (b) corresponding to the [001] projection of $\text{VOHPO}_4 \cdot 0.5\text{H}_2\text{O}$; (d, e, f) VPD-BO precursor material: (d) SEM micrograph showing a rosette-type morphology; (e) BF-TEM micrograph showing a single ‘petal’ from the rosette agglomerate; and (f) SAED pattern from the ‘petal’ in (e) corresponding to the [001] projection of $\text{VOHPO}_4 \cdot 0.5\text{H}_2\text{O}$.

Table 1 Catalytic performance and surface area measurements of the various V-P-O materials for the oxidation of n-butane^c

Catalyst precursor	Activated catalyst	Surface area (m ² g ⁻¹) ^a		n-Butane conversion(%)	Selectivity to maleic anhydride (%)	Intrinsic activity ^b /10 ⁻⁵ (mol m ⁻² h ⁻¹)
		Precursor	Catalyst			
VPD-B (Route A)	VPD-B-c	27	32	50	61	0.96
VPD-BO (Route A)	VPD-BO-c	18	27	50	58	1.09
VPD-OB (Route B)	VPD-OB-c	22	20	29	59	0.87
VPD-M (Route C)	VPD-M-c	17	24	47	55	1.09

^a All samples were degassed for an hour at 120 °C before BET analysis and were labeled according to Scheme 1. ^b Intrinsic activity: moles maleic anhydride formed/m² catalyst/h. ^c Reaction conditions: 400 °C, 1.7% n-butane in air, GHSV = 2000 h⁻¹.

These octagonal structures are typically 4–10 μm in size, and SAED analysis confirms them to be VOPO₄·2H₂O as evidence by the [001] crystal projection shown in Fig. 4(d). The termination facets of the octagonal platelet, each display a 45° intersection angle with adjoining facets, and correspond to alternating {100} and {110}-type planes (Fig. 4(c)). In addition, a small volume fraction of relatively large (~60 μm) flower-like octagonal platelets were found in this VPD-O sample (Fig. 4(b)), which are believed to correspond to the largest square VOPO₄·2H₂O starting platelets (Fig. 1(a), arrowed) that are partway through a delaminating and etching process caused by progressive intercalation of the n-octane. It is known that α₁-VOPO₄ bears some structural similarities to VOPO₄·2H₂O when viewed along the [001] direction, but has a shorter interlayer spacing due to the absence of intercalated water molecules.^{25,26} The delaminated edges in these occasionally found flower-type octagonal platelets (Fig. 4(b)), have probably lost their interlayer water molecules, and possibly locally converted to the α₁-VOPO₄ phase. However the α₁-VOPO₄ phase, if present, is there in such

small quantities that it is below the detectability limits of the XRD and Raman techniques.

The subsequent 2nd stage reflux with 1-butanol causes the reduction of the octagonal VOPO₄·2H₂O plates (V⁵⁺) to the VOHPO₄·0.5H₂O (V⁴⁺). The XRD pattern in Fig. 2 (VPD-OB) exhibits a dominant (001) VOHPO₄·0.5H₂O reflection as opposed to the (220), which is typical of plate-type V-P-O precursors. N₂ BET adsorption measurements (Table 1) reveals that the surface area of VPD-OB is 22 m²g⁻¹. Unlike the rosette agglomerate morphology observed in Route A, nanoscale rhomboidal platelets (Fig. 5(a), (b)) are formed having a typical length of 400–600 nm and thickness of ~40 nm. The SAED pattern obtained from the platelet normal direction corresponds to the [001] VOHPO₄·0.5H₂O projection (Fig. 5(c)), which is consistent with the XRD analysis (Fig. 2, VPD-OB). The edge termination facets exhibited by these rhomboidal platelets corresponded to the {140} and {1̄4 0}-type planes. Clearly the formation of these nanoscale rhomboidal VOHPO₄·0.5H₂O platelets formed *via* route B is a consequence of a different transformation mechanism in comparison with Route A, where rosette formation is preferred.

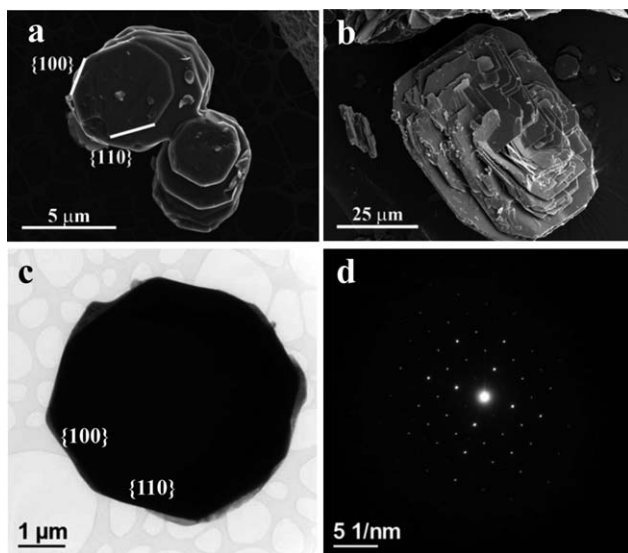


Fig. 4 SEM micrographs of the intermediate VPD-O material (route B) showing (a) the major octagonal platelet morphology and (b) a minor octagonal flower-type morphology; (c) BF-TEM micrograph of sample VPD-O showing alternating {100} and {110} - edge facet termination planes of the octagonal platelets and (d) the corresponding SAED pattern for the particle in (c) which corresponds to [001] VOPO₄·2H₂O.

Electron microscopy characterization of route C material

When VOPO₄·2H₂O is reduced in a single step to VOHPO₄·0.5H₂O by refluxing with a mixture of n-octane and 1-butanol (route C), the morphology of the resulting material (VPD-M) exhibited structural characteristics that were somewhat intermediate between the route A VPD-B rosette-type agglomerates and the route B VPD-OB rhomboidal platelets. VPD-M showed what can be best described as loose rosette-type aggregations of angular platelets (Fig. 6(a)). The BET surface area of VPD-M is only 17 m² g⁻¹ (see Table 1) which is similar to that exhibited by the route B material. TEM analysis confirmed that these angular platelets are the VOHPO₄·0.5H₂O phase which exhibit the [001] projection as the platelet normal (Fig. 6 (b), (c)), which is in good agreement with the corresponding XRD pattern (Fig. 2, VPD-M). Interestingly the (001)/(220) XRD peak ratio has an intermediate value (~1.11) between the highest peak ratio (~2.25) found in VPD-OB (route B) and the lowest ratio (~0.00) in VPD-BO (Route A). This variation suggests the reduced exposure of (001) planes and increased exposure of (220) planes in VPD-M as compared to VPD-OB. The angular platelets in VPD-M when aggregated as shown in Fig. 6(a) could indeed result in a reduced exposure of (001)

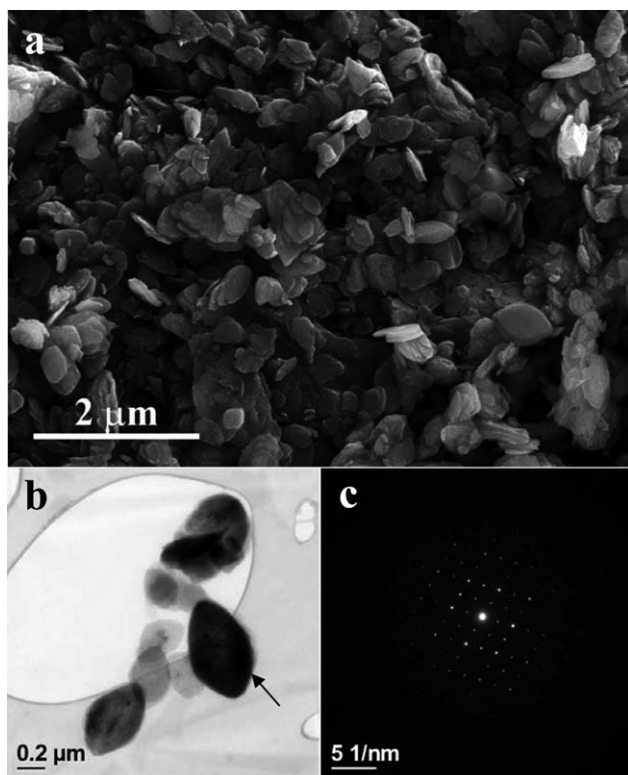


Fig. 5 VPD-OB precursor material produced *via* Route B: (a) SEM micrograph showing nanoscale rhomboidal platelets; (b) BF-TEM micrograph of some nanoscale rhomboidal platelets showing edge termination facets corresponding to {140} and {14 0}-type $\text{VOHPO}_4 \cdot 0.5\text{H}_2\text{O}$ planes and (c) SAED pattern from the platelet arrowed in (b) which corresponds to the [001] projection of $\text{VOHPO}_4 \cdot 0.5\text{H}_2\text{O}$.

$\text{VOHPO}_4 \cdot 0.5\text{H}_2\text{O}$ planes and lead to lowering the (001)/(220) peak ratio.

Comparison of route A, B and C materials as catalysts for n-butane oxidation

The V-P-O catalyst precursors derived from Routes A, B and C were activated and tested in a micro-reactor with 1.7% n-butane/air feed at 400 °C. After 72 h, a steady state production of maleic anhydride was obtained. The catalytic performance data are summarized in Table 1 together with the surface areas of the activated catalysts. As expected, most catalysts display an increase in surface area as compared to their respective precursor materials after catalytic activation. Catalysts VPD-B-c, VPD-BO-c and VPD-M-c all show a similar activity and selectivity to MA, and exhibit comparable specific activity values. Surprisingly, catalyst VPD-OB-c (route B) obtained from the nanoscale rhomboidal catalyst precursor VPD-OB has the lowest specific activity for n-butane conversion at 29%, and is the only material that displays an decrease in surface area after activation.

The XRD patterns of all the activated catalysts are shown in Fig. 7 and all the reflections in each of the patterns can be assigned to vanadyl pyrophosphate, $(\text{VO})_2\text{P}_2\text{O}_7$, which is consistent with the Raman spectra obtained from these materials (Fig. S3, ESI†). Catalysts VPD-B-c and VPD-BO-c display very

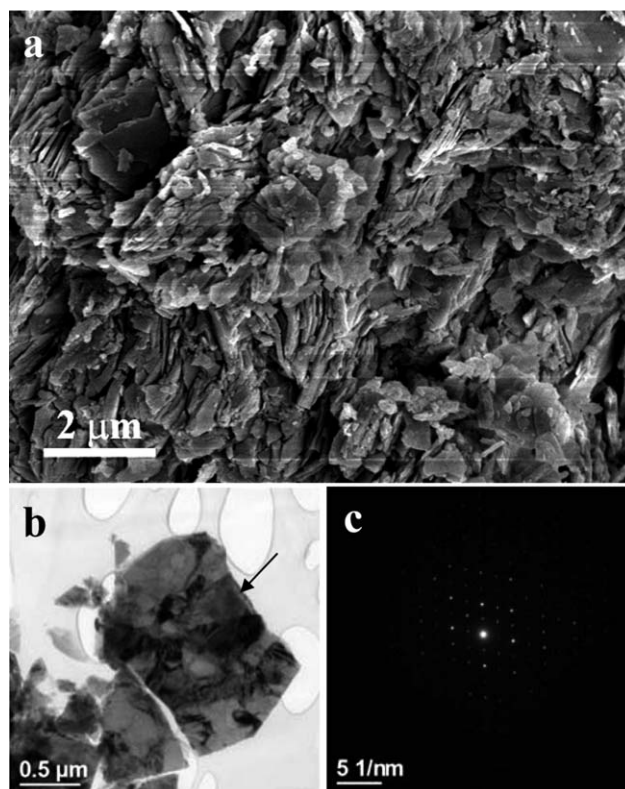


Fig. 6 Precursor material VPD-M derived from route C: (a) SEM micrograph showing rosette-type aggregations of angular platelets; (b) BF-TEM micrograph of a typical angular platelet and (c) SAED pattern from the platelet arrowed in (b) which corresponds to [001] $\text{VOHPO}_4 \cdot 0.5\text{H}_2\text{O}$.

similar XRD patterns having a dominant (024) reflection which is characteristic of rosette-type morphology catalysts. XRD patterns of catalyst VPD-OB-c have relatively broad (200) and (024) peaks indicative of a possible combination of the small primary particle size and the poorly crystalline active $(\text{VO})_2\text{P}_2\text{O}_7$ phase in this sample. The gradually increasing (200)/(024) $(\text{VO})_2\text{P}_2\text{O}_7$ peak ratios observed in Fig. 7 (VPD-B-c \approx VPD-BO-c < VPD-M-c < VPD-OB-c) show a similar trend to the

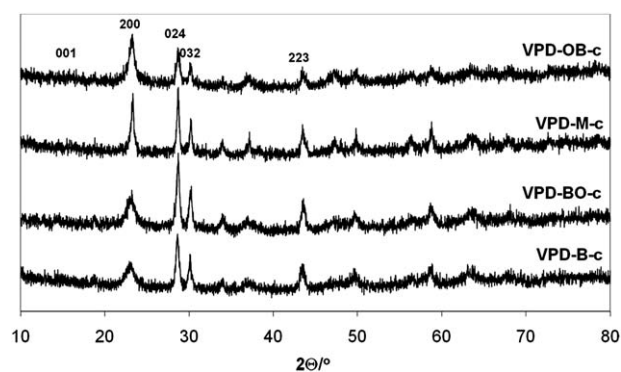


Fig. 7 Powder XRD patterns of the activated catalysts VPD-BO-c (route A), VPD-B-c (intermediate step in route A), VPD-OB-c (final step in route B) and VPD-M-c (route C). All the reflections can be indexed to $(\text{VO})_2\text{P}_2\text{O}_7$.

(001)/(220) $\text{VOHPO}_4 \cdot 0.5\text{H}_2\text{O}$ peak ratios in Fig. 2 (VPD-B \approx VPD-BO < VPD-M < VPD-OB) confirming that a topotactic transformation from $\text{VOHPO}_4 \cdot 0.5\text{H}_2\text{O}$ to the $(\text{VO})_2\text{P}_2\text{O}_7$ phase has occurred. Kiely *et al.*³ have previously studied the structural details of this transformation in which $[001]^{\text{VOHPO}_4 \cdot 0.5\text{H}_2\text{O}}$ is parallel to $[100]^{\text{VO}_2\text{P}_2\text{O}_7}$ and $[010]^{\text{VOHPO}_4 \cdot 0.5\text{H}_2\text{O}}$ is parallel to $[010]^{\text{VO}_2\text{P}_2\text{O}_7}$.

Fig. 8 shows representative SEM micrographs (*row 1*), BF-TEM micrographs (*row 2*) and SAED patterns (*row 3*) obtained from the activated catalysts prepared *via* the three different routes. The morphology of catalyst produced in route A is very similar to that of the corresponding precursor, retaining its characteristic rosette-agglomerate morphology (Fig. 8(a)) as would be expected from the a topotactic transformation of $\text{VOHPO}_4 \cdot 0.5\text{H}_2\text{O}$ to $(\text{VO})_2\text{P}_2\text{O}_7$. SAED patterns from a catalyst “petal” (Fig. 8(b), (c)) can be indexed to the $[100]$ projection of $(\text{VO})_2\text{P}_2\text{O}_7$ ^{27,28} which is consistent with the XRD results presented in Fig. 7- VPD-B-c. Catalyst VPD-OB-c (Fig. 8(d))

displays small crystallites whose size ranges from 50 to 400 nm. A similar morphology was also obtained by Imai *et al.*²³ through activating $340 \text{ nm} \times 35 \text{ nm}$ starting $\text{VOHPO}_4 \cdot 0.5\text{H}_2\text{O}$ crystallites to form the $(\text{VO})_2\text{P}_2\text{O}_7$. SAED patterns from a platelet type aggregate of such particles (Fig. 8(e), (f)) confirm them to be a collection of highly textured, but not perfectly aligned, $(\text{VO})_2\text{P}_2\text{O}_7$ crystallites exhibiting a common $[100]$ normal direction. A representative SEM micrograph of the VPD-M-c catalyst (Fig. 8(g)) also shows aggregations of many smaller particles. Fig. 8(h) and (i) suggest that the small primary particles are $(\text{VO})_2\text{P}_2\text{O}_7$ crystallites with an average size of $\sim 200 \text{ nm}$. The corresponding polycrystalline ring SAED pattern from an agglomerate (Fig. 8(i)) show characteristic (200), (024), and (032) $(\text{VO})_2\text{P}_2\text{O}_7$ reflections and indicate that the primary particles in these agglomerates are more randomly oriented with respect to each other as compared to the route B material.

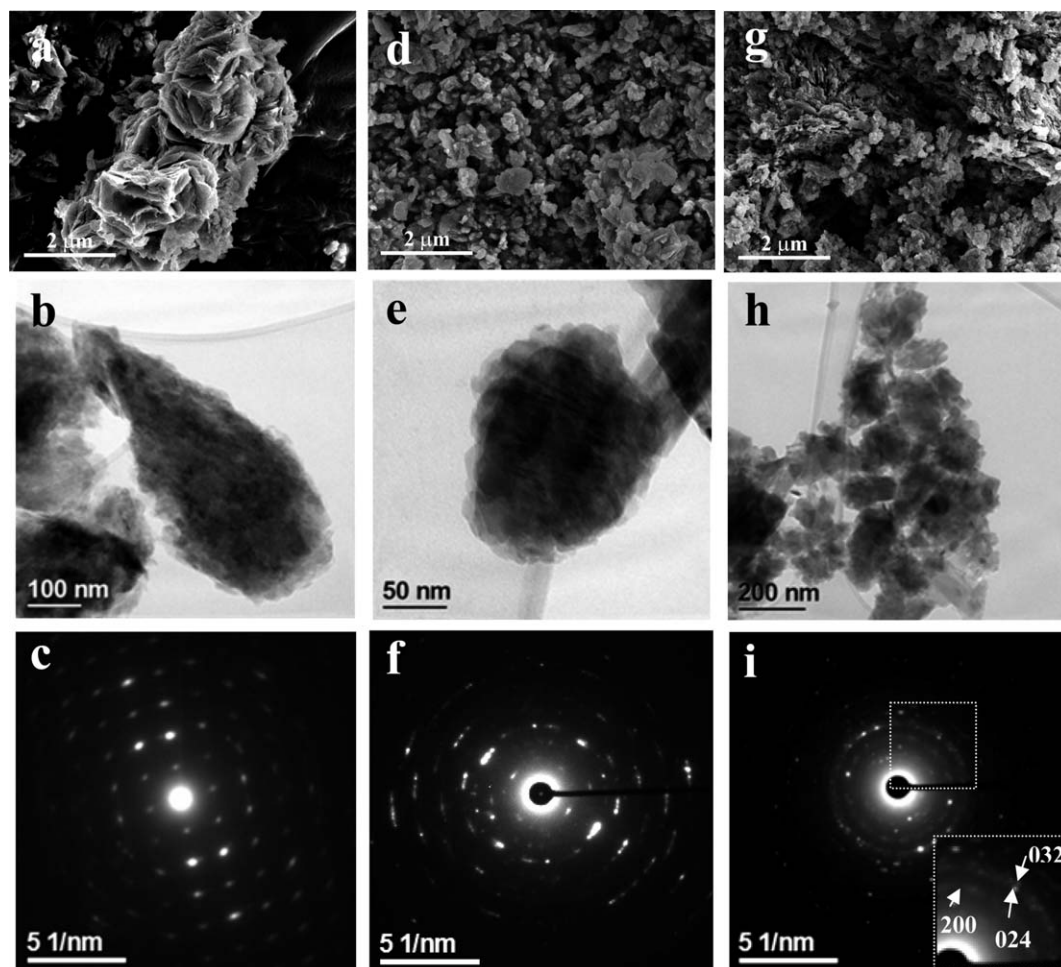
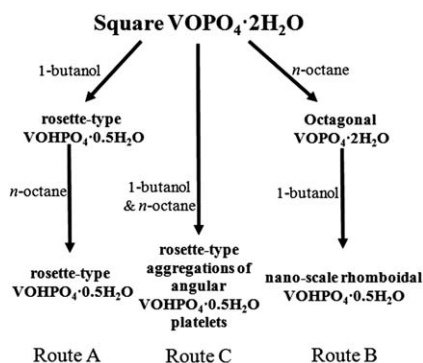


Fig. 8 (a, b, c) Catalyst VPD-B-c (derived *via* route A): (a) SEM micrograph showing a rosette-type agglomerate morphology; (b) BF-TEM micrograph showing a single ‘petal’ from a rosette and (c) the corresponding SAED pattern which can be assigned to the $[100]$ projection of $(\text{VO})_2\text{P}_2\text{O}_7$; (d, e, f) Catalyst VPD-OB-c (derived *via* route B): (d) SEM micrograph showing small agglomerates of particles; (e) BF-TEM micrograph showing an agglomerate of these particles and (f) the corresponding SAED pattern from the collection of particles shown in (e) which can be assigned to several superimposed $[100]$ $(\text{VO})_2\text{P}_2\text{O}_7$ patterns from particles having a relatively high degree of texture; (g, h, i) Catalyst VPD-M-c (derived *via* route C): (g) SEM micrograph showing almost random aggregations of small particles; (h) BF-TEM micrograph showing an aggregation of several small particles and (i) the corresponding SAED ring pattern which can be assigned to almost randomly oriented polycrystalline $(\text{VO})_2\text{P}_2\text{O}_7$ (The inset shows an enlargement of a portion of the ring pattern delineated by the square box showing arcs corresponding to (200), (024) and (032) reflections of $(\text{VO})_2\text{P}_2\text{O}_7$).

Discussion

The order in which the alcohol or alkane (*i.e.*, 1-butanol or *n*-octane) has been added during the co-solvent reduction of square $\text{VOPO}_4 \cdot 2\text{H}_2\text{O}$ platelets has a profound influence on the morphology of the $\text{VOHPO}_4 \cdot 0.5\text{H}_2\text{O}$ precursor generated. Here, we have shown *via* route A that without pre-exposure to *n*-octane, the product consists of typical rosette-type $\text{VOHPO}_4 \cdot 0.5\text{H}_2\text{O}$ agglomerates. Furthermore, *n*-octane added after the reduction with 1-butanol does not significantly change the morphology of the $\text{VOHPO}_4 \cdot 0.5\text{H}_2\text{O}$ material. By way of contrast, analysis of the route B preparation method, show that pre-refluxing the square platelet $\text{VOPO}_4 \cdot 2\text{H}_2\text{O}$ with *n*-octane leads to the formation of partly delaminated octagonal $\text{VOPO}_4 \cdot 2\text{H}_2\text{O}$ platelets. Reduction of this intermediate material with 1-butanol forms distinctive nanoscale rhomboidal $\text{VOHPO}_4 \cdot 0.5\text{H}_2\text{O}$ platelets. Finally, using a mixture of *n*-octane and 1-butanol mixture (route C) reconstructs the square $\text{VOPO}_4 \cdot 2\text{H}_2\text{O}$ platelets into a rosette-type agglomerate of angular $\text{VOHPO}_4 \cdot 0.5\text{H}_2\text{O}$ platelets. All these morphological and structural alterations are summarized in Scheme 2 and can be rationalized to some extent by the different actions of *n*-octane and 1-butanol on the $\text{VOPO}_4 \cdot 2\text{H}_2\text{O}$ crystallites. The *n*-octane predominantly etches the $\text{VOPO}_4 \cdot 2\text{H}_2\text{O}$ crystals altering their morphology, whereas the 1-butanol has a strong intercalation and exfoliation effect on $\text{VOPO}_4 \cdot 2\text{H}_2\text{O}$ and induces its reduction to $\text{VOHPO}_4 \cdot 0.5\text{H}_2\text{O}$. In each case, these precursors, when activated under reaction conditions, convert to the active $(\text{VO})_2\text{P}_2\text{O}_7$ phase and show good activity and selectivity to MA. The VPD-OB-c catalyst derived from the route B nanoscale rhomboidal precursor shows a lower specific activity possibly due to its poorer crystallinity and more limited exposure of the active (100) $(\text{VO})_2\text{P}_2\text{O}_7$ plane.¹ The observed morphology of the VPD-OB-c catalyst also supports this notion as it shows small irregular, but strongly textured $(\text{VO})_2\text{P}_2\text{O}_7$ particles, instead of the more sharply angular and better exposed crystallites normally found in fully activated rosette or platelet type catalyst.²³

It is well known that the catalytically active pyrophosphate phase, $(\text{VO})_2\text{P}_2\text{O}_7$, is obtained by activating a hemihydrate precursor ($\text{VOHPO}_4 \cdot 0.5\text{H}_2\text{O}$) under reaction conditions. The details of the $\text{VOHPO}_4 \cdot 0.5\text{H}_2\text{O}$ to $(\text{VO})_2\text{P}_2\text{O}_7$ topotactic structural transformation that occurs during this activation process have been solved previously by electron microscopy.³ The VPD



Scheme 2 Summary of the morphological and structural features exhibited by this systematic set of samples.

route used in this work for preparing the $\text{VOHPO}_4 \cdot 0.5\text{H}_2\text{O}$ precursor involves reacting V_2O_5 with H_3PO_4 to form the layered (V^{5+}) dihydrate phase ($\text{VOPO}_4 \cdot 2\text{H}_2\text{O}$), which is then subsequently reduced using an alcohol to form the $\text{VOHPO}_4 \cdot 0.5\text{H}_2\text{O}$ precursor (a V^{4+} phase). The structural details of this $\text{VOPO}_4 \cdot 2\text{H}_2\text{O}$ to $\text{VOHPO}_4 \cdot 0.5\text{H}_2\text{O}$ structural transformation are poorly documented and deserve some discussion here.

As shown in Scheme 2, the morphological change to rosette type material occurring during the reduction of $\text{VOPO}_4 \cdot 2\text{H}_2\text{O}$ to $\text{VOHPO}_4 \cdot 0.5\text{H}_2\text{O}$ by 1-butanol (route A) can be explained by the mechanism postulated by O'Mahony *et al.*²⁹ In their proposed scenario, the layered $\text{VOPO}_4 \cdot 2\text{H}_2\text{O}$ material is delaminated by intercalation of the alcohol to form curled $\text{VOPO}_4 \cdot 2\text{H}_2\text{O}$ sheets due to the internal strain. The $\text{VOHPO}_4 \cdot 0.5\text{H}_2\text{O}$ phase is then nucleated at those curled sheet edges until eventually the whole sheet is transformed. The sheets remain connected to some extent during this process leading to the formation of rosette type agglomerates. We have also demonstrated by simple experimentation that a shorter chain alcohol gives a stronger delaminating effect on the layered $\text{VOPO}_4 \cdot 2\text{H}_2\text{O}$ material as shown in Fig. 9. After treatment with ethanol $\text{VOPO}_4 \cdot 2\text{H}_2\text{O}$ (Fig. 9(a)) shows a much greater delamination of the crystallite edges as compared to the material treated with longer chain alcohols (*i.e.*, 1-butanol, Fig. 9(c)).

The square platelets of $\text{VOPO}_4 \cdot 2\text{H}_2\text{O}$ clearly tend to be reformed into rosette-type $\text{VOHPO}_4 \cdot 0.5\text{H}_2\text{O}$ agglomerates (Scheme 2, route A). In comparison, octagonal $\text{VOPO}_4 \cdot 2\text{H}_2\text{O}$, generated *via* route B, preferentially form nanoscale rhomboidal $\text{VOHPO}_4 \cdot 0.5\text{H}_2\text{O}$ platelets (Scheme 2, route B). In order to further understand this difference between routes A and B, both square and octagonal $\text{VOPO}_4 \cdot 2\text{H}_2\text{O}$ materials were exposed to 1-butanol at room temperature (Fig. 10). After 1 min treatment with 1-butanol both types of $\text{VOPO}_4 \cdot 2\text{H}_2\text{O}$ platelets show a slight delamination at their edges (Fig. 10(a), (c)). A closer look at the octagonal $\text{VOPO}_4 \cdot 2\text{H}_2\text{O}$ (VPD-B) platelet shows that it has exhibited small (~ 400 nm) fragments (Fig. 10(b)) that have

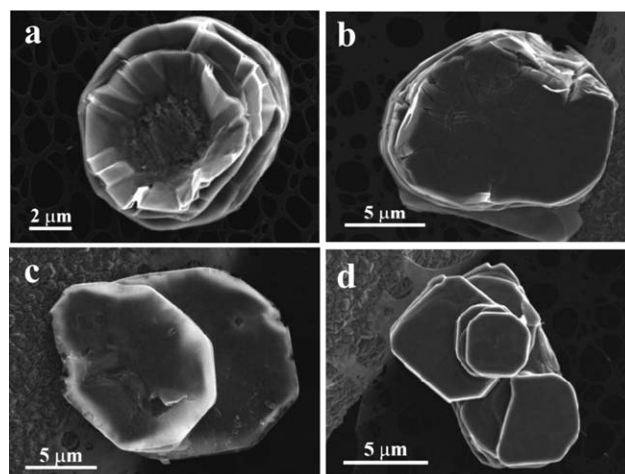


Fig. 9 SEM micrographs of the same $\text{VOPO}_4 \cdot 2\text{H}_2\text{O}$ (VPD-O) material exposed to different alcohols: (a) $\text{C}_2\text{H}_6\text{O}$, (b) $\text{C}_3\text{H}_8\text{O}$, (c) $\text{C}_4\text{H}_{10}\text{O}$ and (d) $\text{C}_5\text{H}_{12}\text{O}$ for 1 min at room temperature showing progressively lower degrees of delamination to the crystallite edges with increasing chain length of the alcohol.

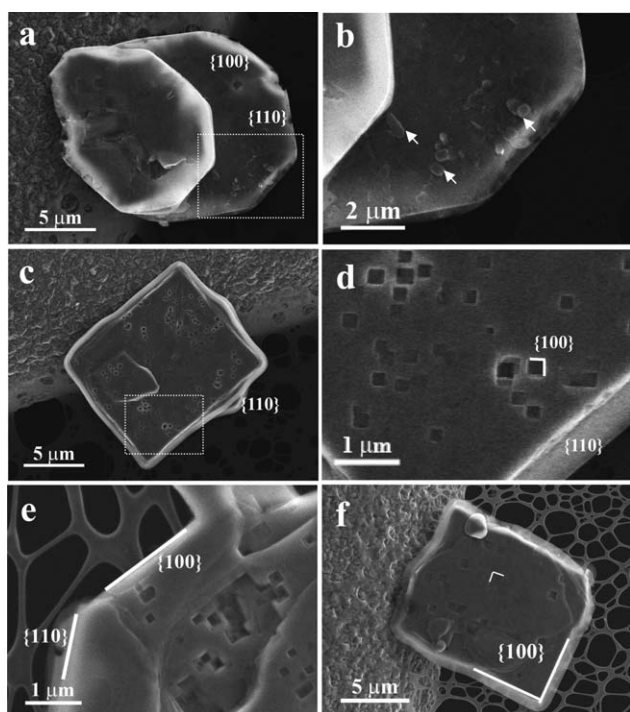


Fig. 10 (a and b): SEM micrographs of octagonal $\text{VOPO}_4 \cdot 2\text{H}_2\text{O}$ platelets showing (a) slight delamination at their edges and (b) the generation of small (~ 400 nm) dissociated surface fragments after 1 min exposure in 1-butanol; (c and d): SEM micrographs of square $\text{VOPO}_4 \cdot 2\text{H}_2\text{O}$ platelets after 1 min exposure in 1-butanol showing (c) slight delamination at their edges and (d) square etch pits with $\{100\}$ -facet walls; (e and f): (e) a typical morphology showing both $\{100\}$ - and $\{110\}$ -type termination facets after 20 min and (f) an occasionally found example having only $\{100\}$ -type termination facets after 60 min.

completely peeled away from the surface which are of a comparable scale to the resulting platelets of $\text{VOHPO}_4 \cdot 0.5\text{H}_2\text{O}$ precursor. This structural transformation in this latter case can be understood by invoking a similar initial mechanism to that proposed for the rosette-type $\text{VOHPO}_4 \cdot 0.5\text{H}_2\text{O}$ formation. However in this instance, the $\text{VOPO}_4 \cdot 2\text{H}_2\text{O}$ sheets are not only delaminated but also prone to fracture into smaller fragments, presumably because of structural defects introduced into the sheets. These fragments subsequently transform into the nano-scale rhomboidal $\text{VOHPO}_4 \cdot 0.5\text{H}_2\text{O}$ platelets. On the other hand, the standard square $\text{VOPO}_4 \cdot 2\text{H}_2\text{O}$ materials develop small square etch pits with $\{100\}$ -type facet walls after 1 min exposure in 1-butanol (Fig. 10(c), (d)). With increasing exposure time to

1-butanol the original $\{110\}$ -type edge termination facets of the $\text{VOPO}_4 \cdot 2\text{H}_2\text{O}$ crystal are gradually eroded and replaced with $\{100\}$ -edge facets (Fig. 10(e)). After 60 min n-butanol exposure, $\text{VOPO}_4 \cdot 2\text{H}_2\text{O}$ platelets having only $\{100\}$ -type edge termination facets and deep etch pits into their surface are observed (Fig. 10(f)). During the reduction reaction with n-butanol, the interlayer water molecules in $\text{VOPO}_4 \cdot 2\text{H}_2\text{O}$ need to escape from the structure. The deep penetrating $\{100\}$ -type etch pits observed in square platelets could open up convenient channels or vents along the $\langle 100 \rangle$ direction of the $\text{VOPO}_4 \cdot 2\text{H}_2\text{O}$ crystallite which facilitate the escape of the interlayer water molecules. In contrast, equivalent $\langle 100 \rangle$ -type channels are not opened up by n-butanol treatment of the octagonal $\text{VOPO}_4 \cdot 2\text{H}_2\text{O}$ platelets probably because of interference from the n-octane molecules introduced during the pre-treatment step. In this latter case, the need to release the trapped interlayer water molecules drives cracking and fracture of the platelets, resulting in the formation of fragments which break away from the structure.

It is well known that both the $\text{VOPO}_4 \cdot 2\text{H}_2\text{O}$ and $\text{VOHPO}_4 \cdot 0.5\text{H}_2\text{O}$ platelets exhibit a layer-type morphology having basal planes with $[001]$ platelet normals as noted above (*i.e.*, $[001]^{\text{VOPO}_4 \cdot 2\text{H}_2\text{O}}$ remains oriented parallel to $[001]^{\text{VOHPO}_4 \cdot 0.5\text{H}_2\text{O}}$ during the transformation). The presence or absence of exposed

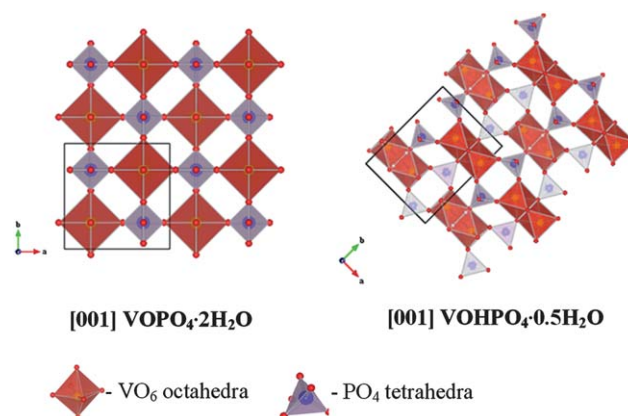


Fig. 12 Atomic structure models of the $\text{VOPO}_4 \cdot 2\text{H}_2\text{O}$ (left) and $\text{VOHPO}_4 \cdot 0.5\text{H}_2\text{O}$ (right) phases oriented in such a way as to be faithful to the experimentally determined epitaxial orientation relationship: $[001]^{\text{VOPO}_4 \cdot 2\text{H}_2\text{O}} // [001]^{\text{VOHPO}_4 \cdot 0.5\text{H}_2\text{O}}$ and $[100]^{\text{VOPO}_4 \cdot 2\text{H}_2\text{O}} // [110]^{\text{VOHPO}_4 \cdot 0.5\text{H}_2\text{O}}$ (red spheres- O, blue spheres- P, yellow spheres- V; red octahedra- VO_6 octahedra, blue tetrahedra- PO_4 tetrahedra; H atoms are omitted for simplicity).

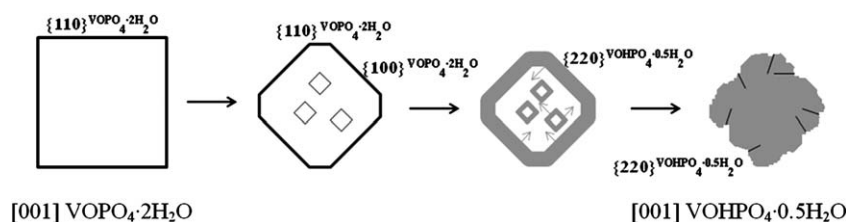


Fig. 11 Schematic illustration of the transformation sequence from a square sheet of $\text{VOPO}_4 \cdot 2\text{H}_2\text{O}$ to rosette-type $\text{VOHPO}_4 \cdot 0.5\text{H}_2\text{O}$ during the reduction step involving 1-butanol (viewed along the $[001]$ projection). (The gray area represents the $\text{VOHPO}_4 \cdot 0.5\text{H}_2\text{O}$ phase and the gray arrows show the growth directions of the $\text{VOHPO}_4 \cdot 0.5\text{H}_2\text{O}$ phase.)

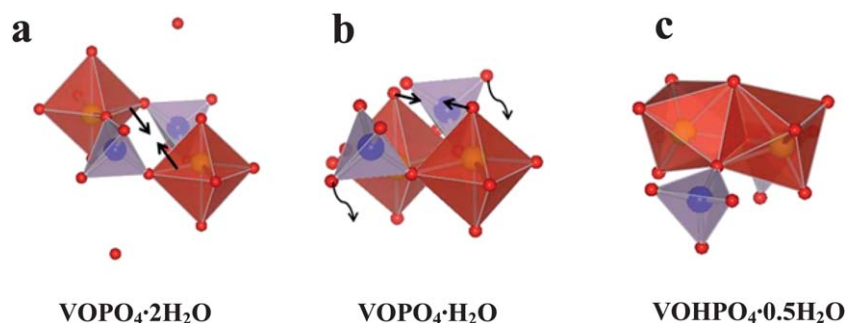


Fig. 13 Structural models of the fundamental building blocks of the (a) $\text{VOPO}_4 \cdot 2\text{H}_2\text{O}$, (b) $\text{VOPO}_4 \cdot \text{H}_2\text{O}$ and (c) $\text{VOHPO}_4 \cdot 0.5\text{H}_2\text{O}$ structures. (red spheres- O, blue spheres- P, yellow spheres- V; red octahedra- VO_6 octahedra, blue tetrahedra- PO_4 tetrahedra; H atoms are omitted for simplicity). The diagram illustrates the proposed mechanism by which (i) unconnected neighbouring VO_6 octahedral units become edge sharing and (ii) edge shared VO_6 octahedral units become face sharing and PO_4 tetrahedral units re-orient during the topotactic transformation from $\text{VOPO}_4 \cdot 2\text{H}_2\text{O}$ to $\text{VOHPO}_4 \cdot 0.5\text{H}_2\text{O}$.

{100}-type (*i.e.*, $(100)^{\text{VOPO}_4 \cdot 2\text{H}_2\text{O}}$ and $(010)^{\text{VOPO}_4 \cdot 2\text{H}_2\text{O}}$) facet planes and etch pits during the alcohol reduction/dehydration stage of the $\text{VOPO}_4 \cdot 2\text{H}_2\text{O}$ material seems to be very important in determining the morphology of the resulting $\text{VOHPO}_4 \cdot 0.5\text{H}_2\text{O}$ precursor (Scheme 2). When these specific {100} facet planes and etch pits are exposed, they can apparently be easily attacked by 1-butanol, resulting in a rosette type $\text{VOHPO}_4 \cdot 0.5\text{H}_2\text{O}$ morphology having (220) planes dominating the XRD patterns and consisting of crystalline ‘petals’ having (220) termination facets. Those {100}-type termination facets and etch pit edges in $\text{VOPO}_4 \cdot 2\text{H}_2\text{O}$ might be the nucleation sites for $\text{VOHPO}_4 \cdot 0.5\text{H}_2\text{O}$ formation and eventually epitaxially convert into the (220) termination facets of $\text{VOHPO}_4 \cdot 0.5\text{H}_2\text{O}$. This proposed scenario is shown in Fig. 11, which is in agreement with previous work by O’Mahony *et al.*²⁹

In this study we have determined that {100}-type planes of $\text{VOPO}_4 \cdot 2\text{H}_2\text{O}$ can epitaxially transform to the (220) planes of $\text{VOHPO}_4 \cdot 0.5\text{H}_2\text{O}$. In addition, we know that the initial $[100]^{\text{VOPO}_4 \cdot 2\text{H}_2\text{O}}$ direction is parallel to the final $[110]^{\text{VOHPO}_4 \cdot 0.5\text{H}_2\text{O}}$ direction. Hence, the full orientation relationship that exists between the $\text{VOPO}_4 \cdot 2\text{H}_2\text{O}$ and $\text{VOHPO}_4 \cdot 0.5\text{H}_2\text{O}$ phases is: $[001]^{\text{VOPO}_4 \cdot 2\text{H}_2\text{O}} // [001]^{\text{VOHPO}_4 \cdot 0.5\text{H}_2\text{O}}$ and $[100]^{\text{VOPO}_4 \cdot 2\text{H}_2\text{O}} // [110]^{\text{VOHPO}_4 \cdot 0.5\text{H}_2\text{O}}$ as illustrated schematically in Fig. 12. The $\text{VOPO}_4 \cdot 2\text{H}_2\text{O}$ structure is known to consist of non-connected VO_6 octahedra interlinked by PO_4 tetrahedra in each tetragonal ‘ VOPO_4 ’ layer.¹⁹ These layers, which are stacked along the [001] direction, are connected by water molecules as shown in Fig. 13(a). However, the sheets in the final $\text{VOHPO}_4 \cdot 0.5\text{H}_2\text{O}$ structure (Fig. 13(c)), are composed of pairs of face sharing VO_6 octahedra that are interlinked by PO_4 tetrahedra.^{4,5,24} These layers are held along the [001] direction through the residual interlayer water molecules. The transformation from $\text{VOPO}_4 \cdot 2\text{H}_2\text{O}$ to $\text{VOHPO}_4 \cdot 0.5\text{H}_2\text{O}$ structure can be envisaged to occur in the following sequence of steps. Firstly, pairs of adjacent VO_6 octahedra shuffle towards one another in a coordinated fashion along the $[110]^{\text{VOPO}_4 \cdot 2\text{H}_2\text{O}}$ direction (as indicated by the arrows in Fig. 13(a)) and connect together such that they share a common edge. To facilitate this, two oxygen atoms are lost from one octahedral unit in the pair. This can also be viewed as one P–O–V bond being broken for every tetrahedral PO_4 group, leaving an unshared corner oxygen in the PO_4 tetrahedral unit. Meanwhile, one water molecule that

is hydrogen bonded to each PO_4 group escapes from the structure giving rise to a transient $\text{VOPO}_4 \cdot \text{H}_2\text{O}$ monohydrate phase (Fig. 13(b)). Indeed, this transient monohydrate phase has previously been detected by O’Mahony *et al.*²⁹ during *in-situ* XRD analysis of the dehydration of $\text{VOPO}_4 \cdot 2\text{H}_2\text{O}$. Next the connected pairs of VO_6 octahedral units in the monohydrate structure re-orient to become face-sharing and yet another oxygen atom is lost from each octahedral pair (which then becomes incorporated into another escaping water molecule). Simultaneously, the V^{5+} cations within each of the VO_6 octahedral units must reduce to the V^{4+} valence state in order to ensure charge neutrality. The final result is that the $\text{VOHPO}_4 \cdot 0.5\text{H}_2\text{O}$ structure is topotactically generated which preferentially exposes the $(001)^{\text{VOHPO}_4 \cdot 0.5\text{H}_2\text{O}}$ basal plane.

Conclusions

The specific *order* in which the alkane and alcohol (*i.e.*, n-octane and 1-butanol) are added to $\text{VOPO}_4 \cdot 2\text{H}_2\text{O}$ in the VPD process has a profound effect on the resultant precursor morphology and can influence the eventual activity of the final $(\text{VO})_2\text{P}_2\text{O}_7$ catalyst. Here we have shown that without n-octane, the reduction product using 1-butanol is the rosette-type $\text{VOHPO}_4 \cdot 0.5\text{H}_2\text{O}$ agglomerate which is the typical precursor to the industrial catalyst. The addition of n-octane after this reduction step does not significantly change the morphology of this precursor. In contrast, the addition of n-octane prior to the alcohol addition results in the formation of distinctive octagonal $\text{VOPO}_4 \cdot 2\text{H}_2\text{O}$ platelets, which are then subsequently reduced by 1-butanol to form nanoscale rhomboidal $\text{VOHPO}_4 \cdot 0.5\text{H}_2\text{O}$ platelets. On the other hand, co-addition of n-octane and 1-butanol can reduce and reform the square $\text{VOPO}_4 \cdot 2\text{H}_2\text{O}$ crystals into a rosette-like aggregates of angular $\text{VOHPO}_4 \cdot 0.5\text{H}_2\text{O}$ platelets. Nearly all the catalysts produced show a good activity and selectivity to maleic anhydride, except for the pyrophosphate material generated from the nanoscale rhomboidal $\text{VOHPO}_4 \cdot 0.5\text{H}_2\text{O}$ platelets, which is probably due to their poorer crystallinity and more limited exposure of the active (100) $(\text{VO})_2\text{P}_2\text{O}_7$ plane.

Additionally, through this study we have identified spatial orientation relationship between the $\text{VOPO}_4 \cdot 2\text{H}_2\text{O}$ and $\text{VOHPO}_4 \cdot 0.5\text{H}_2\text{O}$ crystalline phases, with $[001]^{\text{VOPO}_4 \cdot 2\text{H}_2\text{O}} // [001]^{\text{VOHPO}_4 \cdot 0.5\text{H}_2\text{O}}$ and $[100]^{\text{VOPO}_4 \cdot 2\text{H}_2\text{O}} // [110]^{\text{VOHPO}_4 \cdot 0.5\text{H}_2\text{O}}$. This information has enabled

us to propose a two-step mechanism by which the topotactic VOPO₄·2H₂O to VOHPO₄·0.5H₂O phase transformation occurs. The pairs of adjacent VO₆ octahedra in VOPO₄·2H₂O become edge-sharing in the first step and then become face-sharing in the second step, losing interlayer water molecules at each stage, to form VOHPO₄·0.5H₂O.

Acknowledgements

The authors gratefully acknowledge financial support from the NSF/EPSRC - Materials World Network Program (Grant # DMR-0709887). The atomic structural models presented in Figs. 12 and 13 were generated using the VESTA software package.³⁰

References

- V. V. Guliants, J. B. Benziger, S. Sundaresan, I. E. Wachs, J. M. Jehng and J. E. Roberts, *Catal. Today*, 1996, **28**, 275.
- V. V. Guliants, S. A. Holmes, J. B. Benziger, P. Heaney, D. Yates and I. E. Wachs, *J. Mol. Catal. A: Chem.*, 2001, **172**, 265.
- C. J. Kiely, A. Burrows, G. J. Hutchings, K. E. Bere, J. C. Volta, A. Tuel and M. Abon, *Faraday Discuss.*, 1996, **105**, 103.
- E. Bordes, P. Courtine and J. W. Johnson, *J. Solid State Chem.*, 1984, **55**, 270.
- J. W. Johnson, D. C. Johnston, A. J. Jacobson and J. F. Brody, *J. Am. Chem. Soc.*, 1984, **106**, 8123.
- G. Centi, *Catal. Today*, 1993, **16**, 5.
- R. Al Otaibi, W. Weng, J. K. Bartley, N. F. Dummer, C. J. Kiely and G. J. Hutchings, *ChemCatChem*, 2010, **2**, 443.
- Z. Lin, W. Weng, C. J. Kiely, N. F. Dummer, J. K. Bartley and G. J. Hutchings, *Catal. Today*, 2010, **157**, 211.
- U. Sithamparappillai, J. Luque Nuno, N. F. Dummer, W. Weng, C. J. Kiely, J. K. Bartley and G. J. Hutchings, *J. Mater. Chem.*, 2010, **20**, 5310.
- W. S. Dong, J. K. Bartley, N. F. Dummer, F. Girgsdies, D. S. Su, R. Schlögl, J. C. Volta and G. J. Hutchings, *J. Mater. Chem.*, 2005, **15**, 3214.
- Y. H. Taufiq-Yap, A. R. M. Hasbi, M. Z. Hussein, G. J. Hutchings, J. Bartley and N. Dummer, *Catal. Lett.*, 2006, **106**, 177.
- N. Yamamoto, N. Hiyoshi and T. Okuhara, *Chem. Mater.*, 2002, **14**, 3882.
- Y. Kamiya, S. Ueki, N. Hiyoshi, N. Yamamoto and T. Okuhara, *Catal. Today*, 2003, **78**, 281.
- G. J. Hutchings, M. T. Sananes, S. Sajip, C. J. Kiely, A. Burrows, I. J. Ellison and J. C. Volta, *Catal. Today*, 1997, **33**, 161.
- E. A. Lombardo, C. A. Sanchez and L. M. Cornaglia, *Catal. Today*, 1992, **15**, 407.
- C. J. Kiely, A. Burrows, S. Sajip, G. J. Hutchings, M. T. Sananes, A. Tuel and J. C. Volta, *J. Catal.*, 1996, **162**, 31.
- H. S. Horowitz, C. M. Blackstone, A. W. Sleight and G. Teufer, *Appl. Catal.*, 1988, **38**, 193.
- I. J. Ellison, G. J. Hutchings, M. T. Sananes and J. C. Volta, *J. Chem. Soc., Chem. Commun.*, 1994, 1093.
- H. R. Tietze, *Aust. J. Chem.*, 1981, **34**, 2035.
- T. Yatabe, M. Nakano and G. E. Matsubayashi, *J. Mater. Chem.*, 1998, **8**, 699.
- M. M. Lara, L. M. Real, A. J. Lopez, S. B. Gamez and A. R. Garcia, *Mater. Res. Bull.*, 1986, **21**, 13.
- L. Benes, K. Melanova, V. Zima, J. Kalousova and J. Votinsky, *Inorg. Chem.*, 1997, **36**, 2850.
- H. Imai, Y. Kamiya and T. Okuhara, *J. Catal.*, 2007, **251**, 195.
- M. E. Leonowicz, J. W. Johnson, J. F. Brody, H. F. Shannon and J. M. Newsam, *J. Solid State Chem.*, 1985, **56**, 370.
- L. Benes, K. Melanova, M. Trchova, P. Capkova and P. Matejka, *Eur. J. Inorg. Chem.*, 1999, 2289.
- E. Bordes, P. Courtine and G. Pannetie, *Ann. Chim.*, 1973, **8**, 105.
- P. T. Nguyen, R. D. Hoffman and A. W. Sleight, *Mater. Res. Bull.*, 1995, **30**, 1055.
- C. J. Kiely, S. Sajip, I. J. Ellison, M. T. Sananes, G. J. Hutchings and J. C. Volta, *Catal. Lett.*, 1995, **33**, 357.
- L. O'Mahony, J. Henry, D. Sutton, T. Curtin and B. K. Hodnett, *Appl. Catal., A*, 2003, **253**, 409.
- K. Momma and F. Izumi, *J. Appl. Crystallogr.*, 2008, **41**, 653.